Analyst

ROYAL SOCIETY OF CHEMISTRY

PAPER

View Article Online
View Journal | View Issue

Cite this: *Analyst*, 2025, **150**, 4558

A target-triggered self-assembly QFRP strategy for *in situ* single molecule imaging of intracellular mRNAs

Binxiao Li,*[a,b] Lan Xu,[a] Zesong Jiang,[a] Ruolin Yang[b] and Baohong Liu *[b]

Precise visualization of scarce mRNA transcripts is hindered by the limited performance of conventional probes and the complexity of the intracellular milieu. Here, we present a target-triggered self-assembly-based single quantum dot (QD) fluorescence resonance energy transfer (FRET) probe system (QFRP) for high-resolution mRNA imaging in diverse living cell lines. Compared with conventional single-fluorophore probes, the QFRP exhibits substantially enhanced sensitivity and quantitative accuracy, achieving a detection limit as low as 35 fM while markedly suppressing false positives through dual-signal colocalization. By leveraging QDs as photostable donors and assembled Cy5 acceptors, the QFRP enables effective visualization of subtle differences in mRNA expression between cancerous and normal cells, revealing essential biological heterogeneity in complex intracellular environments. These findings demonstrate the robustness, specificity, and versatility of this single-entity FRET-based nanosystem, underscoring its potential for advanced molecular imaging and precision medicine, particularly in the visual analysis of low-abundance targets within complex microenvironments related to tumor progression.

Received 5th August 2025,
Accepted 2nd September 2025

DOI: 10.1039/d5an00831j

rsc.li/analyst

Introduction

Monitoring of abnormalities in tumor-related genes in living cells provides important information for cancer diagnosis and treatment, and can help to improve patient survival rates.[1] The heterogeneous expression pattern of tumor-associated messenger ribonucleic acids (mRNAs) can reveal unique insights into the molecular mechanisms of tumor progression and prognosis,[2–9] acting as key components and pivotal references for gene therapy, including genetic engineering, infectious disease vaccines and protein replacement.[10,11] However, the low abundance of certain genes and the complex intracellular environment pose significant challenges for accurate mRNA monitoring in living cells.[12] While previous methods, such as RNA sequencing (RNA-seq), polymerase chain reaction (PCR), and northern blotting, have advanced our understanding of mRNA action mechanisms,[1,12–14] they still suffer from limitations in sensitivity, spatial resolution, and real-time monitoring for targeted analysis in current practical analytical requirements. These methods often fail to capture mRNA information at the single-cell resolution and require cell lysis or fixation. Bulk detection of intracellular targets often lead to the omission of inter-target or inter-cell heterogeneity details, thus hindering the information available for further advancement in micro-exploration.[15,16] And the instability due to signal degradation and the accumulation of interferences in the environment can lead to decreased detection accuracy. Furthermore, an equal signal output (1 : 1) limits the generality of the proposed strategy, especially for *in situ* visual analysis of low-abundance targets.

Because of its remarkable advantages, such as non-average recording, ultrahigh sensitivity, and especially its ability to provide richer heterogeneous information within nanosystems,[17–20] single molecule fluorescence (SMF) imaging has emerged as an ideal means for *in situ* tracking.[21–26] Furthermore, SMF imaging enables precise quantification of target molecules through single-dot counting, offering a straightforward and highly accurate visual quantification method with minimal interference. As a result, it has been widely used for visualizing low-abundance targets, such as certain proteins and nucleic acids.[27–30] Despite these superior features, single molecule-based fluorescence imaging faces limitations, particularly in terms of photobleaching and non-specific interference, which compromise measurement precision. The inherent optical properties of single-dye nanoprobes, such as organic dyes or carbon dots, often result in low signal-to-noise ratios due to the presence of intracellular autofluorescence, making single-readout analyses error-prone.

[a]*The Education Ministry Key Lab of Resource Chemistry, College of Chemistry and Materials Science, Shanghai Normal University, Shanghai 200234, China. E-mail: bxli@shnu.edu.cn*
[b]*Department of Chemistry, Shanghai Stomatological Hospital, State Key Lab of Molecular Engineering of Polymers, Institutes of Biomedical Sciences, Fudan University, Shanghai 200438, China. E-mail: bhliu@fudan.edu.cn*

To overcome these limitations, semiconductor quantum dots (QDs) have gained widespread adoption in super-resolution bio-imaging and analytical applications, thanks to their outstanding photochemical stability, extended fluorescence lifetimes, and robust photon yields.[31,32] Additionally, QDs' size-tunable photoluminescence and efficient fluorescence resonance energy transfer (FRET) capabilities enable the design of advanced signal-amplified biosensors for the targeted detection of low-abundance biomarkers.[33–35] By leveraging the FRET between a single donor and multiple acceptor chromophores, the emission intensity can be significantly enhanced, effectively improving the signal-to-noise ratio. Furthermore, QD-based imaging systems can employ single-laser excitation to generate target-specific colocalization signals, thereby minimizing false positives and increasing the accuracy of measurements. In addition to rigorous accuracy and high sensitivity, we hypothesize that an ideal biomolecular analysis strategy can also transform low-abundance targets into highly refined measurable outputs, without altering the normal intracellular physiology.

In this study, we designed a QD-based FRET reporter probe (QFRP) by target-triggered self-assembly for *in situ* real-time monitoring of target c-myc mRNA (Scheme 1). The substrate sequence (SS) modified on the QDs' surfaces initially formed a stable double-stranded structure by complementing with complementary sequence 1 (CS1) and complementary sequence 2 (CS2). Then, c-myc mRNA, as the target trigger, could recognize the SS and gradually replace CS1 to form a SS-mRNA-CS2 intermediate. Furthermore, the intermediate can combine with an engine sequence (ES) modified with a Cy5 fluorophore, which is followed by replacement of the mRNA and CS2 sequence to form a stable SS–ES double-sequence structure. In this way, Cy5 fluorescent molecules were continuously modified on the surface of QDs. With excitation at 488 nm, effective FRET could occur, and the electron energy was transmitted from the QDs to the Cy5 molecules, generating a donor–acceptor type enhanced signal. Additionally, the QDs could function not only as donors, but also as local nanoconcentrators to assemble multiple acceptors. Thus, energy transfer would be fully performed, enhancing the FRET efficiency. In parallel, the collected two-color colocalized signal spots minimize potential interference, thereby enhancing both the accuracy and sensitivity of the analysis. Through FRET nanosystem-based single-molecule colocalization imaging, we achieved c-myc mRNA detection at the picomolar level, coupled with precise, high-resolution *in situ* visualization of intracellular mRNA.

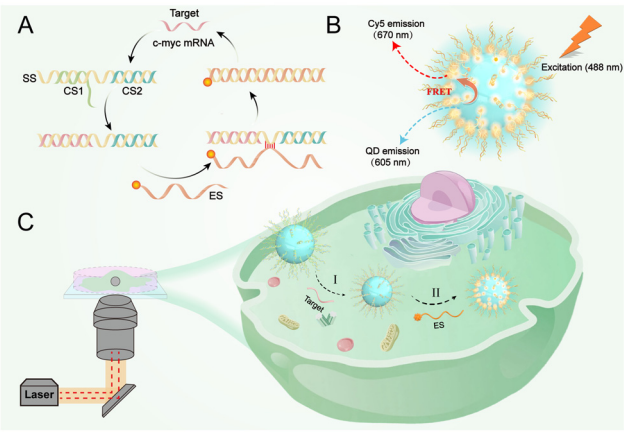

Scheme 1 (A) Structure and design of the QFRP for a c-myc mRNA assay. (B) Mechanism of the FRET between the QDs and Cy5. (C) Schematic diagram of the single-molecule fluorescence imaging platform for *in situ* visualization of mRNA in live cells.

Materials and methods

Preparation of nanoprobes

The SS DNA (1 μM, 50 μL) was added to a 605 QD solution (50 nM, 50 μL) and lightly shaken overnight. Then, by adding the CS1 DNA (1 μM 50 μL) and CS2 DNA (1 μM 50 μL) to the reaction solution, a mild shock reaction was performed for 2 hours, and SS-CS1-CS2@QD was generated. To remove other free SS DNA, CS1 DNA and CS2 DNA, the mixture was centrifuged (30 min, 12 000 rpm) and washed to obtain the nanoprobe (SS-CS1-CS2@QD), which was resuspended in a 1 × Tris–HCl (pH 7.4) solution.

Cell culture and real-time imaging in single cells

All cell lines were grown in a 35 mm^2 glass bottom dish with a 15 mm well and the cell density reached 50–80% after 24 h of culture. Then, to each glass dish, 1 mL of fresh complete medium with serum and antibiotics was added (the manufacturer's protocol notes that antibiotics do not influence the result) 2 h before transfection. Next, the ES DNA (1 μM) and PureFection reagent (6 μL) were added into an Eppendorf tube containing 50 μL of serum-free DMEM. The mixture was vortexed for 5–10 s and incubated for ~15 min at room temperature to allow PureFection/ES DNA complexes to form. Then the SS-CS1-CS2@QD and PureFection/ES DNA complexes (2 nM) were incubated with cells for 3 h. One group of MCF-7 cells seeded with the SS-CS1-CS2@QD and PureFection reagent was used as a control. After gently washing with 1× PBS, the cells were imaged with an oil immersion 100× objective or a common 25× objective.

Imaging experiments and data processing

We performed imaging in a home-built fluorescence monitoring system which had been introduced in our previous study. The 488 nm laser beams were focused and then collimated using an oil immersion objective (100×, NA 1.45, Olympus, Japan) to generate a circular excitation field to excite the nanoprobes on the glass slide surface. The signal of the nanoprobes was obtained using the objective and then separated and steered onto the two halves (two channels) of an EMCCD camera (iXon DU897, Andor Technology Plc., UK) by using a splitter (OptoSplit II, Andor Technology Plc., UK) respectively. For each test, we imaged different parts, each part was con-

tinuously imaged for 30 frames, and the exposure time was 0.1 s. With the MATLAB (MathWorks Inc., MA) program, we analysed the single molecule image, and the area of 40 μm × 20 μm was analysed for each frame. First, we determined the coordinates of signal dots. Second, we counted the signal dots based on the coordinates found in the first step. Finally, we compared and matched all the spots with certain criteria where the matched spots were denoted as valid spots.

Results and discussion

To verify whether mRNA can trigger effective FRET between QDs and Cy5, the fluorescence emission spectra of QDs and Cy5 were analysed (Fig. 1A). Without the target mRNA present, only a fluorescence peak at 605 nm was measured under 488 nm excitation (black curve). In the presence of mRNA under the same excitation, the QD signal peak at 605 nm was weakened, while a Cy5 fluorescence signal peak at 680 nm appeared (red curve). These results indicate that the target mRNA could induce effective FRET between QDs and Cy5. Moreover, we also verified the feasibility of the QFRP design strategy by polyacrylamide gel electrophoresis (PAGE) (Fig. 1B). When the SS sequence (lane 1), CS1 (lane 2), and CS2 (lane 3) were mixed, a SS-CS1-CS2 double-sequence structure formed, resulting in a new band (lane 6). After adding the target mRNA, CS1 was replaced by mRNA to form a new SS-mRNA-CS1 double-sequence structure and generate a corresponding band (lane 7). After further addition of the SS sequence, mRNA and CS2 were gradually replaced to form a stable SS/ES duplex, and the corresponding band was observed in lane 8. It is proved that mRNA can effectively induce the self-assembly of Cy5 signal molecules onto the QD surface.

Leveraging our self-constructed single-molecule fluorescence imaging platform (Fig. S1), we confirmed the feasibility of mRNA co-localization analysis. Under the trigger of c-myc mRNA, the ES strand modified with the Cy5 molecule and the SS sequence formed a stable double-sequence structure on the QD surface, thereby enabling efficient FRET between Cy5 and QDs. With only 488 nm laser (QD excitation light) excitation, the Cy5 signal can be visualized in parallel, generating signal spots. As shown in Fig. 1C, when the target mRNA was absent, fluorescence signal dots were uniformly distributed in the QD signal channel, while only a few false-positive signals caused by non-specific adsorption were collected in the Cy5 signal channel. This indicates that Cy5 molecules were not specifically assembled on the QD surface, and no FRET occurred between QDs and Cy5. However, when c-myc mRNA was added, fluorescence signal spots were captured in both channels, and QD (green spot) and Cy5 (red spot) signals were almost perfectly co-localized, demonstrating that mRNA could successfully initiate the self-assembly process of the QFRP. Then, Cy5 fluorophores were continuously modified on the surfaces of QDs and effective FRET between QDs and Cy5 occurred. Moreover, the QFRP shows excellent stability and

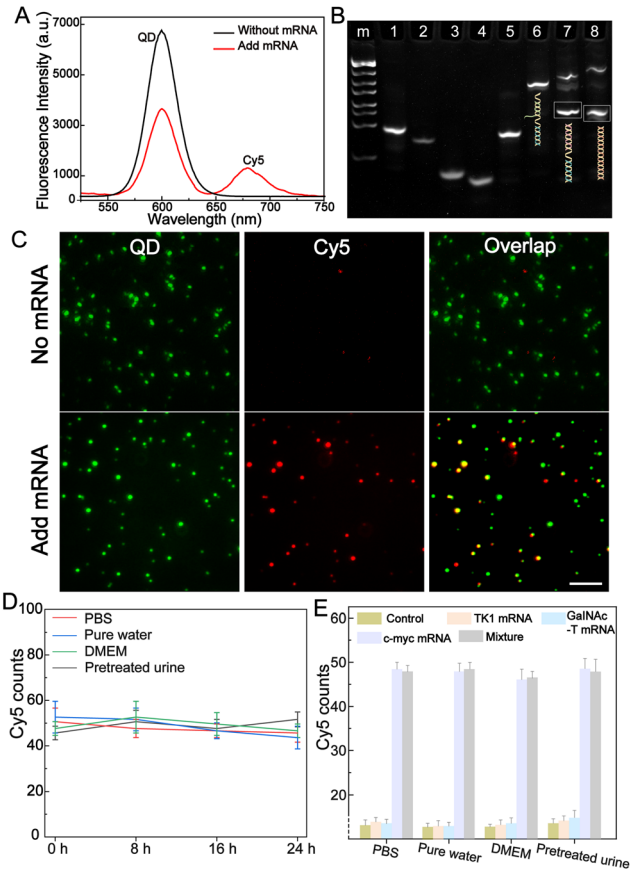

Fig. 1 (A) Fluorescence emission spectra of the QFRP in the presence (red line) and absence (black line) of mRNA. (B) The gel electrophoresis analysis of the assembling process of the QFRP. Lane 1: SS DNA, lane 2: CS1 DNA, lane 3: CS2 DNA, lane 4: c-myc mRNA, lane 5: ES DNA, lane 6: a mixture of SS, CS1, and CS2, lane 7: a mixture of SS, CS1, and CS2 + target mRNA, and lane 8: a mixture of SS DNA/mRNA + ES DNA. (C) Single molecule fluorescence images of the QFRP in the absence and presence of mRNA. The mRNA concentration is 5 pM. The signal points of QDs are shown in green. The signal spots of Cy5 are displayed in red. The overlap signal points are shown in yellow. The scale bar is 5 μm. (D) The stability verification of the QFRP in different environments, and (E) the detection ability of the QFRP in complex environments. The serum and urine were pretreated with c-myc mRNA. The mixture includes TK1 mRNA, GalNAc-T mRNA and c-myc mRNA. The error bars show the standard deviations of three independent experiments.

detection capabilities in complex environments (Fig. 1D and E), ensuring the smooth progress of subsequent experiments.

After optimizing a series of experimental conditions (Fig. S2), we evaluated the sensitivity of the constructed sensing platform by imaging mRNA molecules at different concentrations. Moreover, to minimize sampling errors, three identical samples were measured for each concentration, and more than ten different areas were taken for each sample. As expected, as the mRNA concentration increased, the Cy5 signal counts gradually increased (Fig. 2), suggesting that the mRNA could effectively induce FRET between the QDs and Cy5 fluorescent molecules. Furthermore, in order to eliminate the presence of impurity signal spots, we used fluorescence co-localiz-

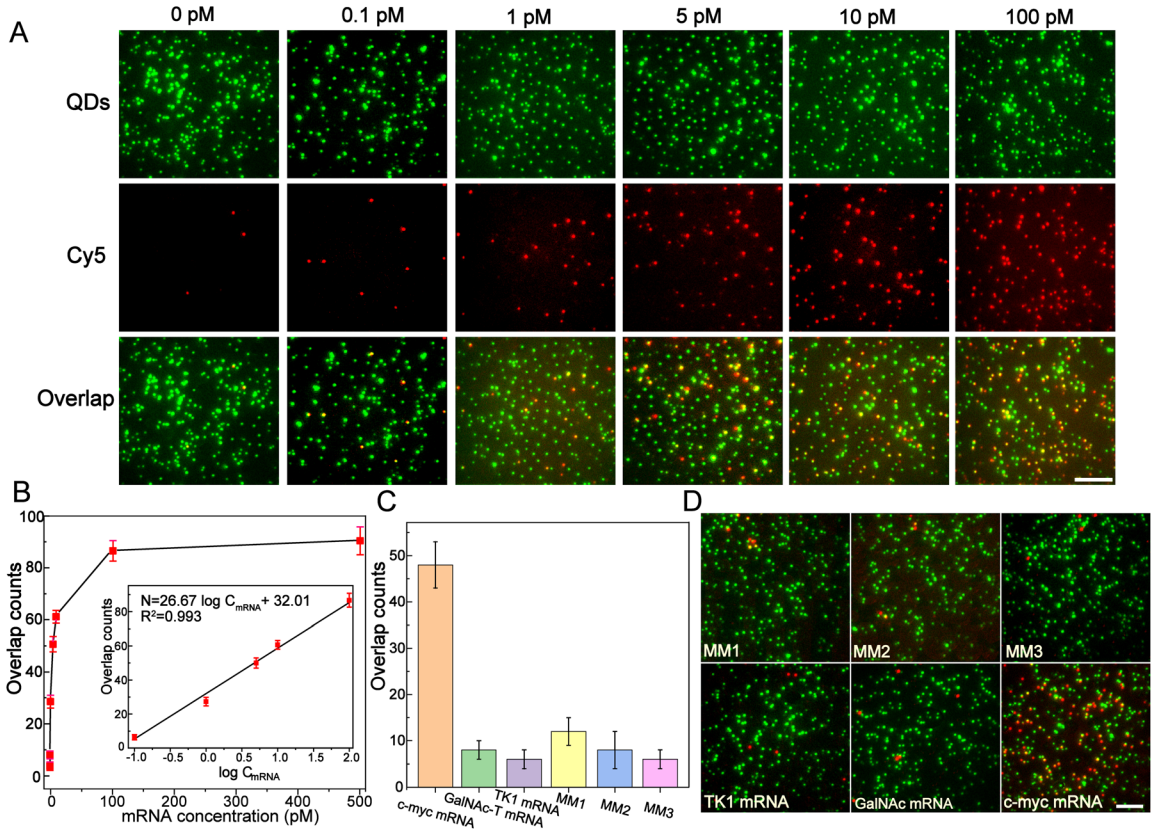

Fig. 2 (A) Single molecule fluorescence images of the QFRP with different concentrations of c-myc mRNA. The scale bar is 5 μm. (B) Linear relationship between overlap counts and the logarithm of c-myc mRNA concentration in the range from 0 pM to 100 pM. (C) The specificity measurement of the QFRP detection strategy and (D) the overlapping images. The concentration of each interferent is 10 pM. The target mRNA is 10 pM. Error bars indicate means ± SD (n = 3).

ation analysis. By choosing the overlap of Cy5 and QD fluorescence spots as effective signals, we can achieve accurate counting of target-triggered signal spots. Using statistical analysis of the two-color signal spots at different mRNA concentrations, we found that there was a desirable linear relationship between the overlap spots and the logarithm of mRNA concentration in the range of 0.1 pM to 100 pM (Fig. 2B). The regression equation is $N = 26.67 \log C + 32.01$ ($R^2 = 0.993$), where C represents the mRNA concentration (pM) and N represents the number of overlaps. The detection limit of this nanosystem was determined to be 35 fM based on the mean signal of the blank sample plus three times the standard deviation. Compared with other detection methods, our strategy shows excellent performance with a wide detection range and a low detection limit (Table S1). For the purpose of testing the selectivity of the present strategy, we used a variety of oligonucleotides as interference control groups, including a one base mismatch sequence (MM1), a two base mismatch sequence (MM2), a three base mismatch sequence (MM3), GalNAc-T mRNA, and TK1 mRNA. As shown in Fig. 2C and D, many effective Cy5 fluorescence spots were observed only in the presence of the target group, which sharply contrasted the results of the interference control groups. This illustrates that our imaging strategy has outstanding selectivity for low-abundance biomolecules. Based on these preliminary results, we co-incubated the designed probe with MCF-7 cells to dynamically image mRNA in living cells. Firstly, we used the CCK-8 kit to detect the cytotoxicity of different reagents against MCF-7 cells. As shown in Fig. S3, the cells still maintained a high survival rate after incubation with the constructed reporter probe for 24 h, indicating negligible cytotoxicity of the QFRP.

After MCF-7 cells were incubated with the QFRP and ES DNA for 2 h, fluorescence spots appeared in the QD channel under 488 nm excitation, demonstrating that the QFRP successfully entered the cells (Fig. 3A). The signal spots observed in the Cy5 channel corresponded well with the QD signal spots. The Pearson co-localization coefficient between the QD green and Cy5 red channels was above 0.8 (Fig. 3A). And when the cells were incubated with the QFRP only, the fluorescence spots were present only in the QD channel (Fig. S4). This suggests that the Cy5 fluorescence spots in cells were caused by FRET of the Cy5/QD single-entity triggered *via* the target mRNA.

We further investigated the ability of the QFRP to detect mRNA in other cancer cell lines (HepG2 cells) and non-cancer cell lines (MCF-10A cells, Fig. 3B). Because of the relatively

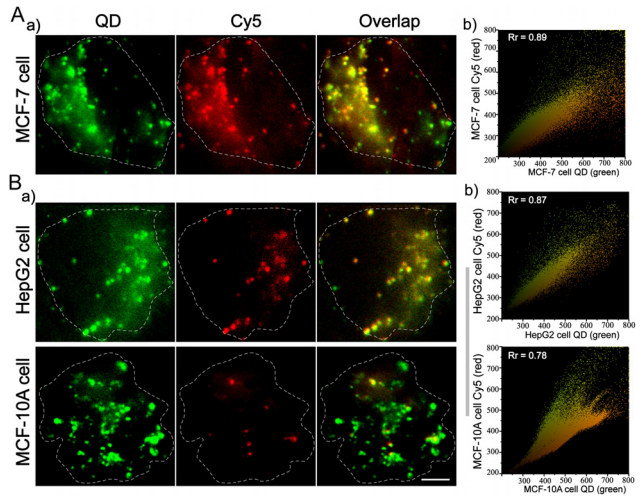

Fig. 3 (A) The single molecule fluorescence images of the QFRP in MCF-7 cells and the colocalization scatter plot and Pearson coefficient for c-myc mRNA *in situ* imaging. (B) The single molecule fluorescence images of the QFRP in HepG2 cells and MCF-10A cells, and the colocalization scatter plots and Pearson coefficients. The scale bar is 5 μm.

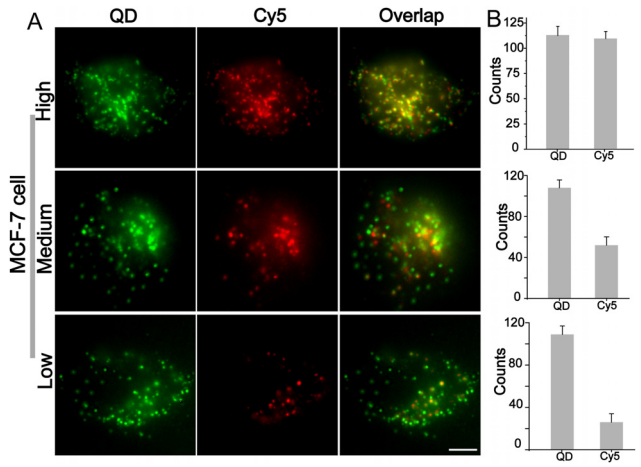

Fig. 4 (A) The single molecule fluorescence images of MCF-7 cells incubated with high, medium and low concentrations of ES DNA in the presence of abundant intracellular QFRP. (B) The number of QDs and Cy5 signal spots in single cells. The scale bar is 5 μm. Error bars indicate means ± SD (n = 20).

higher mRNA expression levels in HepG2 cells, the number of effective Cy5 signal spots was more than that in MCF-10A cells, which is in accordance with the data from statistical analysis (Fig. S5). These results validate that the QFRP can monitor changes in mRNA expression levels in living cells and visually discriminate cell types, especially the cancer and normal cells. Furthermore, when the number of QD signal spots (from the QFRP) remains constant, the number of Cy5 signal spots (from ES DNA) observed in the MCF-7 cells corresponds to changes in ES DNA content (Fig. 4). This correspondence demonstrates the strategy's accuracy for detecting intracellular targets from a visual perspective.

Conclusions

To sum up, we developed a QD-mediated FRET single-molecule imaging platform for visual imaging and sensitive detection of c-myc mRNA *in situ*. In this system, mRNA could successfully trigger the self-assembly of the QFRP through a toehold-mediated strand displacement reaction. Subsequently, under excitation at 488 nm, FRET between QDs and Cy5 molecules occurred, allowing dual-signal co-localized detection. Compared with the traditional single fluorescence signal analysis methods, the QFRP nanosystem performed well in eliminating the false positive signal and improving the accuracy and sensitivity of imaging analysis. Additionally, the constructed imaging platform achieved efficient differentiation of mRNA in various cell lines at the single molecule level. With its robust sensitivity, high specificity, and versatility, this target-induced FRET-based visualization approach represents a promising tool for next-generation molecular imaging and precision medicine applications.

Author contributions

Binxiao Li: Conceptualization, writing – review & editing, data curation. Lan Xu: Conceptualization, formal analysis, investigation, methodology, writing – original draft. Zesong Jiang: Investigation, formal analysis. Ruolin Yang: Investigation, formal analysis. Baohong Liu: Conceptualization, funding acquisition, methodology, project administration, supervision, writing – review & editing.

Conflicts of interest

There are no conflicts to declare.

Data availability

All data generated or analyzed during this study are included in this article and its SI. Supplementary information is available. See DOI: **https://doi.org/10.1039/d5an00831j**.

Acknowledgements

This work was supported by the National Natural Science Foundation of China (NSFC, 21934001, 22025403, 22404026), the Natural Science Foundation of Shanghai (24ZR1455900), the Science and Technology Commission of Shanghai Municipality (25ZR1401018) and the State Key Laboratory of Molecular Engineering of Polymers (Fudan University). The authors thank Prof. J. Liu for his helpful discussions and experimental assistance.

References

1 L. He, D. Q. Lu, H. Liang, S. Xie, C. Luo, M. Hu, L. Xu, X. Zhang and W. Tan, *ACS Nano*, 2017, **11**, 4060–4066.
2 B. Wu, A. R. Buxbaum and R. H. Singer, *Science*, 2014, **343**, 419–422.
3 A. R. Buxbaum, G. Haimovich and R. H. Singer, *Nat. Rev. Mol. Cell Biol.*, 2014, **16**, 95–109.
4 R. Deng, K. Zhang, Y. Sun, X. Ren and J. Li, *Chem. Sci.*, 2017, **8**, 3668–3675.
5 J. Huang, T. Zhang, H. Li, Z. Li, S. Yin, Y. Liu, C. Zhang, Y. Qiu and H. Yu, *Adv. Sci.*, 2025, e01656.
6 P. Le, N. Ahmed and G. W. Yeo, *Nat. Cell Biol.*, 2022, **24**, 815–824.
7 H. Schwarzenbach, D. S. B. Hoon and K. Pantel, *Nat. Rev. Cancer*, 2011, **11**, 426–437.
8 S. Tyagi, *Nat. Methods*, 2009, **6**, 331–338.
9 Y. Xia, R. Zhang, Z. Wang, J. Tian and X. Chen, *Chem. Soc. Rev.*, 2017, **46**, 2824–2843.
10 W. J. Liu, Y. Han, R. Song, F. Ma and C. Y. Zhang, *Anal. Chem.*, 2025, **97**, 8098–8108.
11 Y. Xiao, Z. Tang, X. Huang, W. Chen, J. Zhou, H. Liu, C. Liu, N. Kong and W. Tao, *Chem. Soc. Rev.*, 2022, **51**, 3828–3845.
12 H. M. Yuan, H. J. Li, L. J. Wang and C. Y. Zhang, *Biosens. Bioelectron.*, 2025, **287**, 117728.
13 G. Bao, W. J. Rhee and A. Tsourkas, *Annu. Rev. Biomed. Eng.*, 2009, **11**, 25–47.
14 J. Shi, M. Zhou, A. Gong, Q. Li, Q. Wu, G. J. Cheng, M. Yang and Y. Sun, *Anal. Chem.*, 2016, **88**, 1979–1983.
15 X. H. Xu and E. S. Yeung, *Science*, 1997, **275**, 1106–1109.
16 H. Jung, C. G. Gkogkas, N. Sonenberg and C. E. Holt, *Cell*, 2014, **157**, 26–40.
17 S. Weiss, *Science*, 1999, **283**, 1676–1683.
18 T. Y. A. Ishijima, *Trends Biochem. Sci.*, 2001, **26**, 438–444.
19 P. Holzmeister, G. P. Acuna, D. Grohmann and P. Tinnefeld, *Chem. Soc. Rev.*, 2014, **43**, 1014–1028.
20 A. Sett, L. Zara, E. Dausse and J. J. Toulmé, *Anal. Chem.*, 2020, **92**, 9113–9117.
21 B. X. Li, Y. W. Lu, X. D. Huang, Y. J. Ning, Q. Shi, J. W. Liu and B. H. Liu, *Small*, 2024, **20**, 2305777.
22 A. Yildiz, J. N. Forkey, S. A. Mckinney, T. Ha, Y. E. Goldman and P. R. Selvin, *Science*, 2003, **300**, 2061–2065.
23 X. W. Zhuang, L. E. Bartley, H. P. Babcock, R. Russell, T. Ha, D. Herschlag and S. Chu, *Science*, 2000, **288**, 2048–2051.
24 Q. Qiao, A. Song, K. An, N. Xu, W. Jia, Y. Ruan, P. Bao, Y. Tao, Y. Zhang, X. Wang and Z. Xu, *Angew. Chem., Int. Ed.*, 2025, **64**, e202417469.
25 R. W. K. Chiu, C. R. Cantor and Y. M. D. Lo, *Trends Genet.*, 2009, **25**, 324–331.
26 J. F. T. Ha, S. Schmid, N. K. Lee, R. L. Gonzalez Jr, S. Paul and S. Yeou, *Nat. Rev. Methods Primers*, 2024, **4**, 21.
27 J. Hu, M. H. Liu, Y. Li, B. Tang and C. Y. Zhang, *Chem. Sci.*, 2018, **9**, 712–720.
28 C. Phelps, B. Israels, D. Jose, M. C. Marsh, P. H. Hippel and A. H. Marcus, *Proc. Natl. Acad. Sci. U. S. A.*, 2017, **114**, E3612–E3621.
29 R. C. Somers, M. G. Bawendi and D. G. Nocera, *Chem. Soc. Rev.*, 2007, **36**, 579–591.
30 H. Zhang, Y. Liu, K. Zhang, J. Ji, J. Liu and B. Liu, *Anal. Chem.*, 2018, **90**, 9315–9321.
31 I. L. Medintz, A. R. Clapp, H. Mattoussi, E. R. Goldman, B. Fisher and J. M. Mauro, *Nat. Mater.*, 2003, **2**, 630–638.
32 Y. Zhang, Q. N. Li, K. Zhou, Q. Xu and C. Y. Zhang, *Anal. Chem.*, 2020, **92**, 13936–13944.
33 C. Léger, A. Yahia-Ammar, K. Susumu, I. L. Medintz, A. Urvoas, M. Valerio-Lepiniec, P. Minard and N. Hildebrandt, *ACS Nano*, 2020, **14**, 5956–5967.
34 M. Kurashvili, J. Llusar, L. S. Stickel, T. Würthner, D. Ederle, I. Infante, J. Feldmann and Q. A. Akkerman, *Angew. Chem., Int. Ed.*, 2025, **64**, e202420658.
35 Y. Zhang, Q. N. Li, K. Y. Zhou, Q. F. Xu and C. Y. Zhang, *Anal. Chem.*, 2020, **92**, 13936–13944.